iScience

CellPress
OPEN ACCESS

Article

Electrospun rhodamine@MOF/polymer luminescent fibers with a quantum yield of over 90%

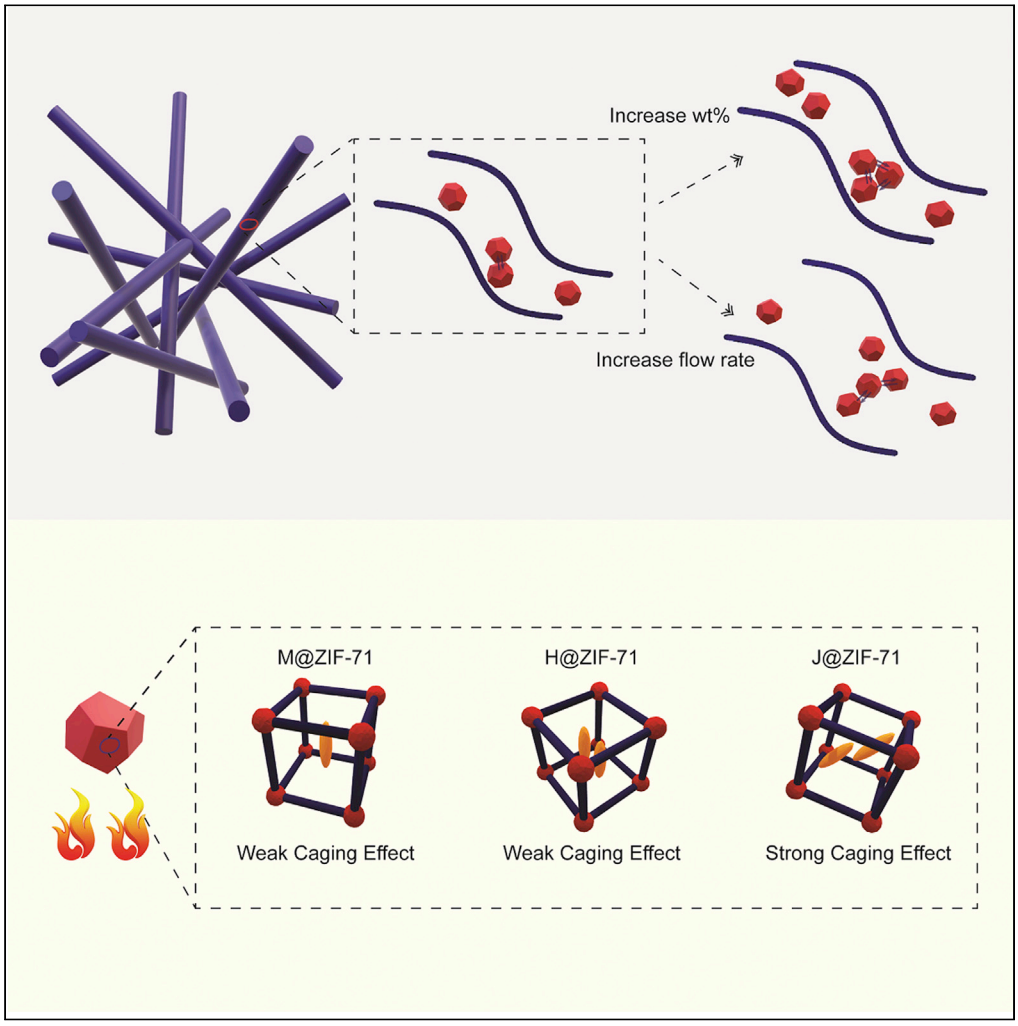

Yang Zhang, Jin-Chong Tan

jin-chong.tan@eng.ox.ac.uk

Highlights

Thermofluorochromic fibers incorporating Guest@MOF engineered by electrospinning

J-aggregates of rhodamine B (RhB) interact through adjacent ZIF-71 nanocrystals

RhB@ZIF-71/PVDF fiber has a quantum yield exceeding 90%

ZIF-71 host enhances the thermal stability of nanoconfined RhB guest

Zhang & Tan, iScience 24, 103035
September 24, 2021
https://doi.org/10.1016/j.isci.2021.103035

iScience

CellPress
OPEN ACCESS

Article

Electrospun rhodamine@MOF/polymer luminescent fibers with a quantum yield of over 90%

Yang Zhang[1] and Jin-Chong Tan[1,2,*]

SUMMARY

Tailored luminescent guest@metal-organic framework (Guest@MOF) materials with outstanding photophysical properties are enabling materials for emergent technologies in smart sensors and optoelectronics. However, the practical utility of Guest@MOF currently is impaired by its poor stability and difficult-to-handle powder form. Here, we combine a luminescent-sensing Guest@MOF system with a non-luminescent polymer matrix and, for the first time, demonstrated the easy-to-apply electrospinning of luminescent fibers comprising nanocrystals of RhB@ZIF-71 (rhodamine B@zeolitic imidazolate framework-71) homogeneously dispersed in a polyvinylidene difluoride (PVDF) matrix. The luminescence of RhB@ZIF-71/PVDF fiber is tunable and exhibits a quantum yield exceeding 90%. Compared with RhB fluorophore in PVDF fiber, the ZIF-71 (host) protects the nanoconfined RhB guest molecules (especially the J-aggregates of RhB), giving the composite fiber its unique thermofluorochromic response and enhanced thermal stability to 200°C. Our results reveal the exciting opportunities for implementing electrospun luminescent fibers functionalized with bespoke Guest@MOF nanocrystals for multifunctional device applications.

INTRODUCTION

Light-emitting materials (LEMs) convert absorbed energy into light; they are therefore central to technological applications and widely integrated into LEDs for lighting and display, fluorescent sensors, bio-imaging, photoswitches, and optoelectronics (Li et al., 2020; Luo et al., 2020; Lustig et al., 2017; Stassen et al., 2017). In recent years, with the advent of device miniaturization, portability, and energy saving requirements of modern optoelectronics, improving the performance of solid-state LEMs has become increasingly demanding (Kamtekar et al., 2010; Kanagaraj et al., 2019). That has stimulated a lot of research on exploring new solid-state LEMs. Among the many new types of solid-state LEMs studied, metal-organic frameworks (MOFs) have been demonstrated as one of the most promising candidate materials for engineering fluorescent optics and sensors because of their porous, ordered, and highly adjustable structure for tunable photophysics and photochemistry (Mollick et al., 2019; Gutiérrez et al., 2021; Chaudhari and Tan, 2020; Aguilera-Sigalat and Bradshaw, 2016; Takashima et al., 2011). In principle, the luminescent properties of MOFs can be designed and controlled by tailoring the molecular building blocks to meet the varied application requirements (Cui et al., 2012; Dolgopolova et al., 2018; Easun et al., 2017; Heine and Muller-Buschbaum, 2013; Yao et al., 2020).

The physical and chemical functions of MOFs can be enhanced further by leveraging the concept of "Guest@MOF" system (Allendorf et al., 2015), yielding luminescent composite materials attractive for solid-state lighting and optical sensing applications (Zhang et al., 2020; Gutiérrez et al., 2020; Chaudhari et al., 2017; Lin et al., 2019). This "guest-host" system takes advantage of the porous nature of MOF (serving as a "host") to confine luminescent molecules (as a "guest") into the nanoscale pores or by trapping them within the extended MOF structures. MOF can apply a caging effect to the nanoconfined guests; this mechanism helps to limit the non-radiative decay of fluorophores and thus improving the guests' luminescent properties (Wang et al., 2019; Tang et al., 2014; Mieno et al., 2016; Hao and Yan, 2015; Asadi et al., 2019). Furthermore, because many MOF structures are themselves also luminescent, the MOF host can form a dual-emission system with the guest or transfer the absorbed energy to the guest, further improving the overall luminescent performance (Dong et al., 2014; Fu et al., 2018; Qin and Yan, 2018; Yoo et al., 2019; Zhao et al., 2018). For example, our research group developed a RhB@ZIF-71 system (i.e., rhodamine B fluorophores confined in zeolitic imidazolate framework-71 host), which not only overcomes the drawback that RhB cannot emit light in the solid-state due to quenching but also endows the material with new

[1]Multifunctional Materials & Composites (MMC) Laboratory, Department of Engineering Science, University of Oxford, Parks Road, Oxford OX1 3PJ, UK

[2]Lead contact

*Correspondence: jin-chong.tan@eng.ox.ac.uk

https://doi.org/10.1016/j.isci.2021.103035

functions, namely mechanochromism, thermochromism, and solvatochromism (Zhang et al., 2020). However, the Guest@MOF materials may suffer from certain shortcomings, especially of poor long-term stability under real-world engineering application conditions. Besides, this material's loose powdery morphology may not be suitable for certain applications, such as optical fibers and precision devices.

To address the outstanding challenges in the field, herein we demonstrate a Guest@MOF material that can be facilely combined with polymers to form a composite, which enables the Guest@MOF material to retain its luminescent properties, enhance thermal stability, and improve its processability so that it can afford practical engineering applications. In this study, we combined RhB@ZIF-71 nanocrystals, as an example, with a PVDF (polyvinylidene difluoride) polymer matrix, which has excellent durability and is non-luminescent, to make easy-to-apply nanofibers by electrospinning technology. Compared with RhB@ZIF-71 powder, we found the composite fibers show a high quantum yield (QY) combined with excellent thermal stability, broadening the application of this Guest@MOF material.

RESULTS AND DISCUSSION

Nanocrystals of RhB@ZIF-71 from high concentration reaction

Recent studies have shown that the nominal size of the RhB@ZIF-71 crystals synthesized by the traditional method is about 800 nm to 1 μm (Yin et al., 2017; Zhang et al., 2020), which is way too large for incorporation into nanofibers (bigger crystals may not to be completely covered by polymer matrix). To reduce the size of the RhB@ZIF-71 crystal, herein we applied the high concentration reaction (HCR) method (see detailed reaction steps in the experimental section). HCR uses a small quantity of solvents to increase the reactants concentration, when coupled with triethylamine (NEt_3) this accelerates the deprotonation of the linkers to enhance nucleation rate and reducing the crystal size (Chaudhari et al., 2017). In contrast to traditional synthesis, which takes many hours to stir the solution during a slow crystallization step, the HCR method yields nanocrystals spontaneously. The Guest@MOF product is formed instantaneously during solution mixing, which considerably shortens the synthesis time and this could benefit future industrial production.

Figure 1 shows the morphology, crystal structure, and the solid-state luminescent properties of the HCR-synthesized RhB@ZIF-71 measured by atomic force microscopy (AFM), powder X-ray diffraction (PXRD), and spectrofluorometry, respectively. From Figures 1A and 1B, it can be seen that the size of the obtained RhB@ZIF-71 nanocrystal is about 50–150 nm. Importantly, the RhB@ZIF-71 retains the crystalline structure of ZIF-71 (Figure 1C) and exhibits the characteristic luminescent properties of the RhB fluorophore (Figure 1D). These unique features of RhB@ZIF-71 provide the opportunity to fabricate nanofibers via electrospinning, as described below.

Morphology and microstructure of electrospun fibers

After dispersing the nanocrystals of RhB@ZIF-71 within the PVDF solution (polymer matrix), we used electrospinning technology to process the composite mixture into RhB@ZIF-71/PVDF nanofibers. SEM images in Figure 2 show that the surface of the obtained fibers exhibits a highly uniform dispersion of nanocrystals coated by the PVDF matrix, and there is no sizable RhB@ZIF-71 aggregate present on the fiber surface. For comparison, the "normal" (without HCR) RhB@ZIF-71/PVDF fibers were made using the same electrospinning technique; the SEM images (Figure S1) revealed that there are many micron-sized crystals and large aggregates prevalent on the fibers.

To confirm that the prepared fibers still retain the functional RhB@ZIF-71 instead of being decomposed or lost during the electrospinning process, we tested the fibers under a UV lamp. Compared to pure PVDF, which is not luminescent, the RhB@ZIF-71 fibers show a distinctive fluorescence (Figures 3A and 3B). This observation proves that the RhB@ZIF-71 is intact in the fiber. Subsequently, we have systematically performed the X-ray diffraction (XRD), ultraviolet-visible (UV-Vis) diffuse reflectance spectroscopy, and attenuated total reflection Fourier-transform infrared spectroscopy (ATR-FTIR) characterization on these fibers (Figure 3). From the XRD patterns in Figure 3C, we can identify the peaks of RhB@ZIF-71/PVDF fibers at 2θ of about 4° and 7.5°; these correspond to the characteristic peaks of the RhB@ZIF-71 nanocrystals. In addition, the appearance of the peaks at ~20° in the PVDF fiber and RhB@ZIF-71/PVDF fiber indicates that the introduction of RhB@ZIF-71 into the polymer matrix has no effect on the transformation of PVDF from α to β phase during electrospinning (Flyagina et al., 2017); this finding suggests that there is no strong interaction between RhB@ZIF-71 and PVDF. From Figures 3D and 3E, we can also get the same inference by observing the similar RhB characteristic absorbance peak between 450 and 600 nm and the FTIR peak of ZIF-71 at 1052 cm^{-1}. We infer that the

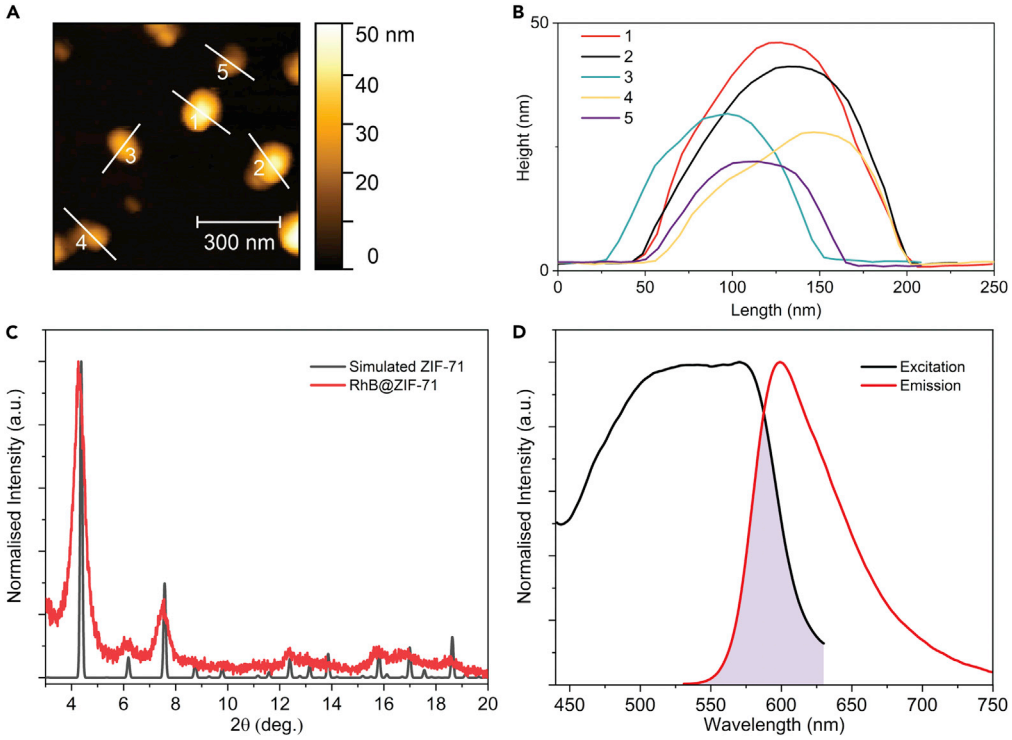

Figure 1. Characterization of RhB@ZIF-71 nanocrystals

(A and B) AFM height topography showing the nominal size of the RhB@ZIF-71 nanocrystals synthesized by the HCR method.

(C) PXRD patterns of RhB@ZIF-71 powder where peak broadening is due to nanocrystals, compared with the simulated pattern of ZIF-71.

(D) Solid-state excitation and emission spectra of the RhB@ZIF-71 powder.

high hydrophobicity originated from the chemical structure of ZIF-71 produces many surface-bound negative charges (Nauruzbayeva et al., 2020), and it is due to this repelling electrostatic effect that RhB@ZIF-71 nanocrystals achieve a relatively uniform dispersion in the PVDF fiber.

Photoluminescent properties of RhB@ZIF-71/PVDF fibers

It is expected that the different processing parameters during electrospinning will modify the fiber properties, which in turn might affect the luminescence behavior of RhB@ZIF-71/PVDF fibers. To investigate this possible effect, we compared the excitation and emission spectra of the electrospun fiber mats containing different mass fractions (wt.%) of RhB@ZIF-71 nanocrystals (Figures 4A and 4B) and those obtained by varying the polymer flow rates (μL/min) through the nozzle (Figures 4C and 4D).

From Figures 4B and 4D, it can be seen that with the increase in the mass fraction and flow rate, the luminescence of RhB@ZIF-71/PVDF fibers yields a redshift. Observing Figures 4A and 4C, we note that the excitation peak became wider and the shoulder to the peak ratio increases, suggesting that with the increase in the mass fraction and flow rate, the number of RhB@ZIF-71 nanocrystals per unit fiber length also rises (Note: for samples with increased flow rate, the reason is due to the larger fiber diameter, see Figure 4D inset and Figures S2–S4). On this basis, the reason for the observed redshift may be associated with more RhB@ZIF-71 crystals causing more interactions between the RhB J-aggregates over the contacting crystal interfaces. This mechanism is similar to the interaction described in the previous literature (Chaudhari and Tan, 2018;Zhang et al., 2020).

Lifetime data determined from time-correlated single-photon counting (TCSPC) measurements (Figure 5, Tables S1 and S2) can help to validate this hypothesis. The time constant τ_2 in Figure 5, Tables S1, and S2, which represents the lifetime of RhB J-aggregates, was found to decrease with the increase of mass fraction and flow rate. This trend indicates a stronger interaction between the J-aggregates. On the other hand, the

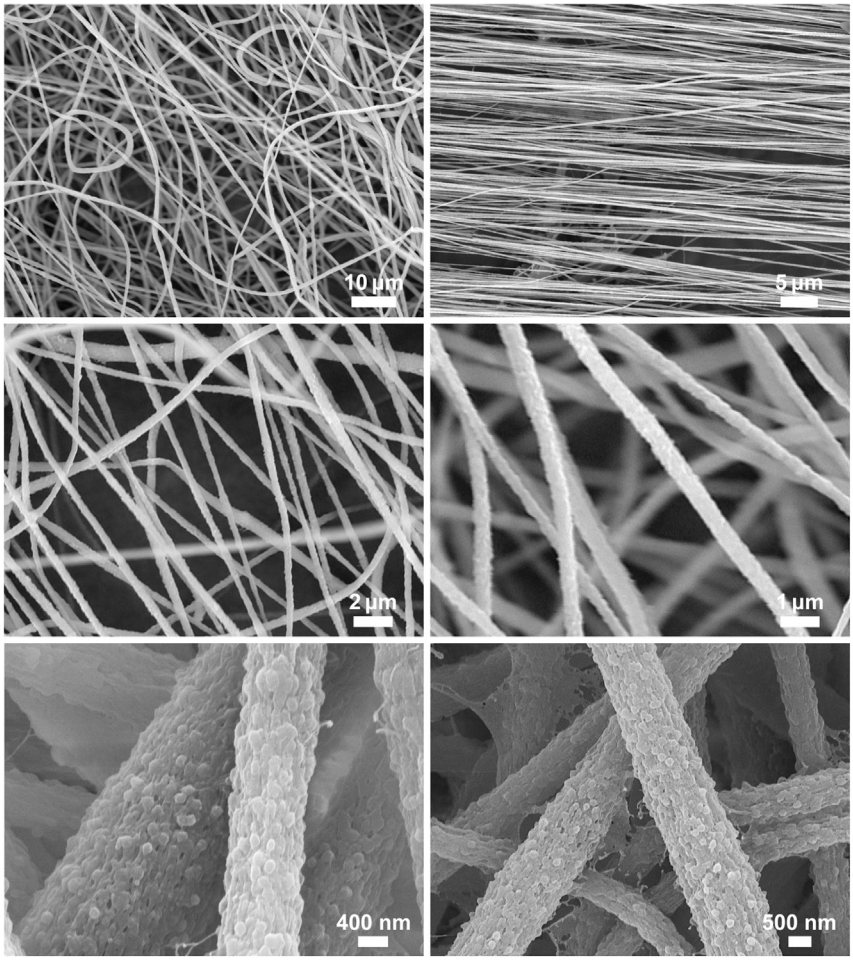

Figure 2. Electron micrographs of electrospun PVDF fibers incorporating RhB@ZIF-71 HCR nanocrystals
The orientation of the individual fibers (random vs aligned) and the overall architecture of fiber mat can be controlled by employing collectors of different geometries. The high-resolution images at the bottom images reveal the uniform dispersion of the HCR nanocrystals coated by the PVDF matrix.

pre-exponential factor and fractional contribution of J-aggregates (a_2 and c_2, respectively) both show higher values as the flow rate increases (Table S2), which we attributed to the stronger caging effect experienced by the J-aggregates. With a faster flow rate, a greater negative impact on RhB luminescence is also anticipated due to the incorporation of residual polar aprotic solvents (i.e. dimethylacetamide (DMA) will turn RhB into the less emissive lactone form) (Zhang et al., 2020; Hinckley et al., 1986). The relatively large J-aggregates will receive a stronger caging effect (Zhang et al., 2020), becoming more difficult to be affected by the solvent molecules (i.e. reducing pore space to accommodate additional solvent molecules) and thus resulting in the increase in the values of a_2 and c_2. The lifetime data therefore enable us to explain why a higher wt.% loading of RhB and/or a higher flow rate will give an emission redshift.

Further to the tunable luminescence elucidated above, another striking feature of RhB@ZIF-71/PVDF fiber is that it exhibits a high QY (Figures 5C and 5D, Tables S3 and S4). Because the caging effect reduces the non-radiative decay of RhB (Zhang et al., 2020; Mieno et al., 2016; Cui et al., 2012) and the introduction of PVDF significantly decreases the self-absorption of well-dispersed RhB@ZIF-71 nanocrystals (ascribed to the overlapping excitation-emission phenomenon, see Figure 1D), we found that the fibers obtained under the conditions of 1 wt.% and 8 μL/min achieve a QY of ~92% (versus QY ~25% in the corresponding bulk powder sample). This value of QY is the highest yet among the MOF-polymer systems reported to date (Zhang et al., 2007; Bai et al., 2018) and when compared against the RhB-based fluorescent materials whose QYs are commonly lying in the relatively lower bound of 30–60% (Table S5) (Ahmed and Saif, 2013;

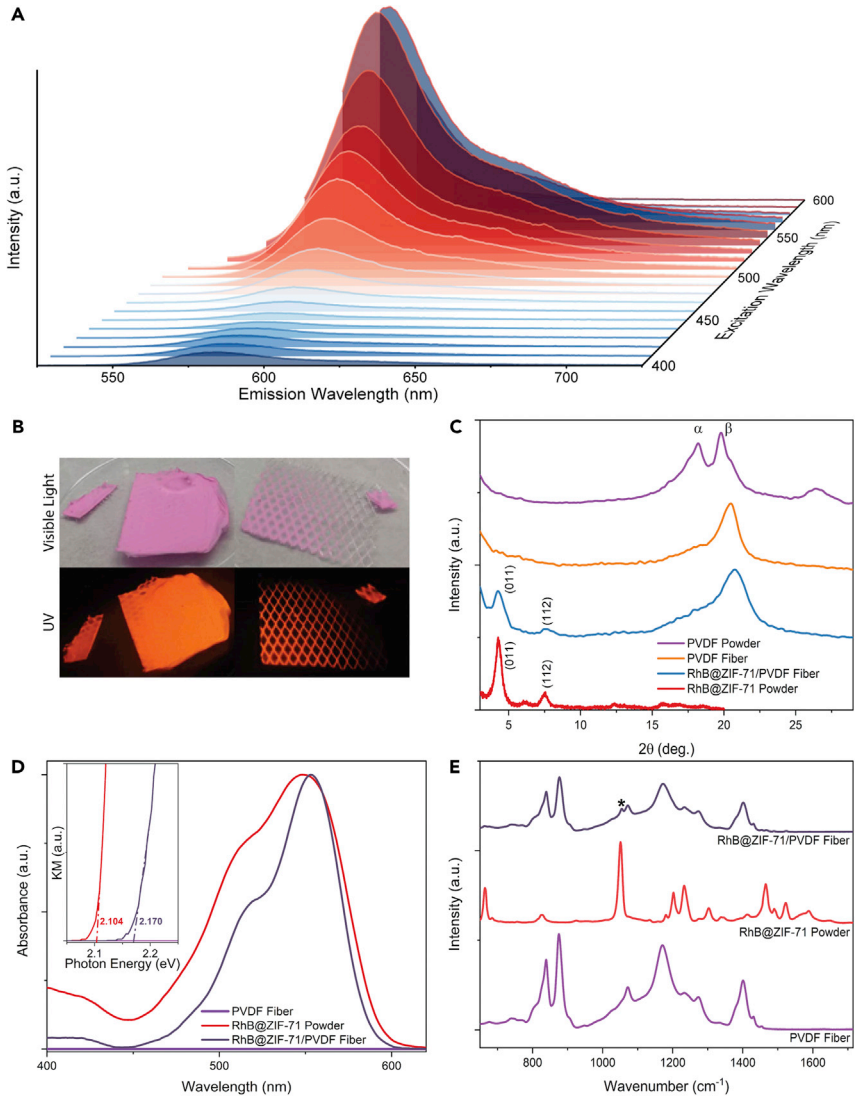

Figure 3. Characterization of RhB@ZIF-71/PVDF fibers

(A and B) (A) Emission map for a range of excitation wavelengths ranging from 400 to 600 nm (B) RhB@ZIF-71/PVDF fiber mats (random and textured) under the visible light and their luminescence under the UV lamp (365 nm excitation). (C–E) (C) XRD, (D) UV-Vis diffuse reflectance spectra (the insert figure is the Kubelka-Munk function for estimating the optical band gaps based on the photon energy intercepts), and (E) ATR-FTIR spectra of RhB@ZIF-71/PVDF fibers, RhB@ZIF-71 HCR powder, and PVDF fibers. The * symbol in (E) denotes the position of the 1052 cm^{-1} peak of ZIF-71.

Khader, 2008; Sagoo and Jockusch, 2011; Stobiecka and Hepel, 2011). Our findings reveal that this high QY fiber can be a promising candidate for optoelectronics and sensing.

Comparison of thermofluorochromic properties between RhB@ZIF-71/PVDF fibers and RhB/PVDF fibers

In order to further study the thermofluorochromic properties of RhB@ZIF-71/PVDF fibers, we focused on the highest QY fiber mat, i.e. RhB@ZIF-71/PVDF prepared under the conditions of 1 wt.% and 8 μL/min, and systematically studied its thermochromism compared with the RhB/PVDF fibers.

From the excitation and emission spectra (Figure S5) of these two kinds of fibers, it is clear that the luminescent properties of the two were similar under ambient conditions. However, under a high-temperature environment, the luminescence of RhB@ZIF-71/PVDF fiber was significantly more stable than the RhB/PVDF

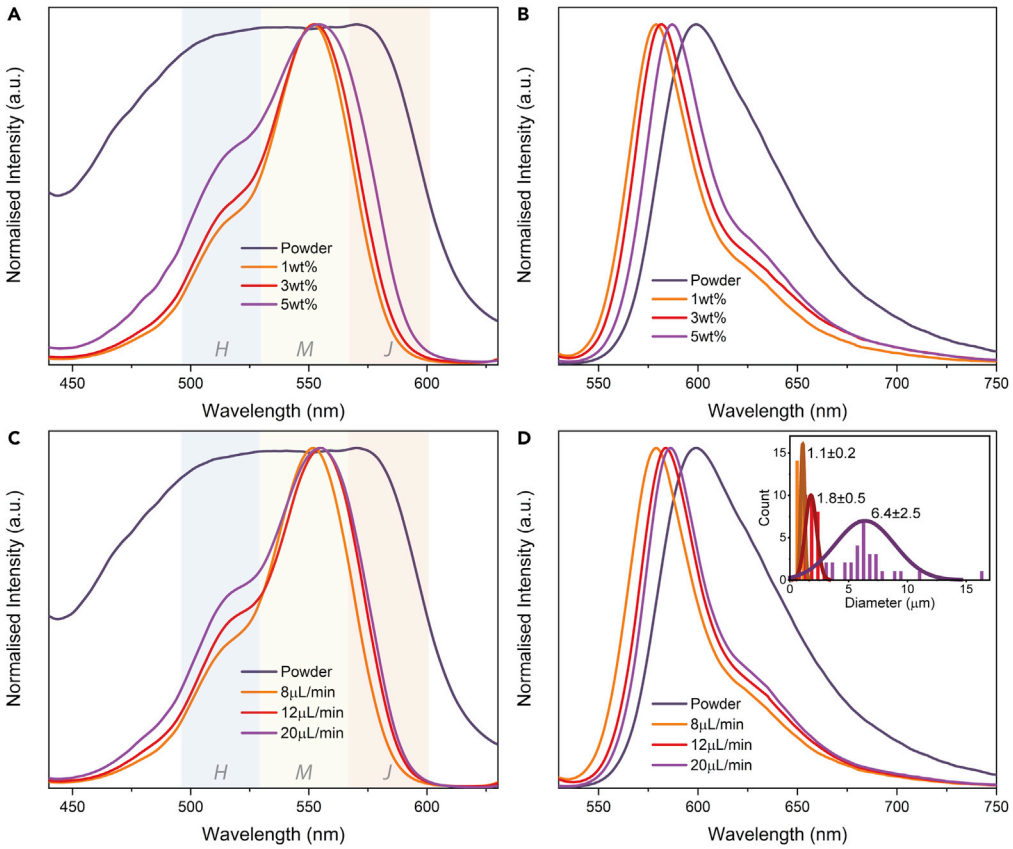

Figure 4. Fluorescent properties of RhB@ZIF-71/PVDF fibers with different processing parameters

Excitation and emission spectra of RhB@ZIF-71/PVDF fibers with different mass fraction of guest loading wt.% (A and B) and by using different PVDF flow rate for electrospinning (C and D), respectively. The spectra of the pristine RhB@ZIF-71 powder are plotted together for contrast. The inset of (D) shows the normal distributions of the fiber diameters associated with the differential flow rates in electrospinning.

fiber. From the excitation and emission spectra measured at different temperatures (Figures 6 and S6), we established that when the temperature was close to 200°C, the RhB@ZIF-71/PVDF fiber still maintains its good RhB luminescence characteristics, but the emission of RhB/PVDF fibers was significantly degraded. This thermally induced material damage can also be seen with the naked eye as depicted in the insets of Figure 6E, showing the luminescent properties of RhB/PVDF are considerably deteriorated after heating to 200°C due to the dramatic increase in non-radiative decay as a function of temperature (Hinckley et al., 1986), and subsequently the molecular decomposition of RhB when approaching 200°C (Zhang et al., 2020).

Moreover, in a gradually heating environment, the RhB@ZIF-71/PVDF fiber showed a systematic redshift (Figures 6B and 6C), and its corresponding excitation (550–600 nm, Figure 6A) exhibited a relative increase in intensity. In contrast, the optical response of RhB/PVDF fiber has no correlation to the temperature at all, see Figure 6D. These phenomena are in line with the conclusions in our previous study: the J-aggregates are subjected to a stronger caging effect in ZIF-71, leading to a relative increase in intensity at high temperature (Zhang et al., 2020), which will result in a luminescent redshift. After cooling, we found that the emission of RhB@ZIF-71/PVDF fiber retained a certain degree of redshift (Figures 6B and 6C), the peak position of its excitation did not change, and the relative intensity of the right shoulder of the excitation (560–580 nm) increased (Figure 6A). These observed characteristics support the notion that the J-aggregates within the RhB@ZIF-71/PVDF fibers are better protected under an elevated temperature. In addition, we observed that the luminescence of RhB@ZIF-71/PVDF fiber was not affected by the melting point of PVDF (Figure S7), notably the luminescence property of RhB is retained after undergoing multicyclic heating (Figure S8). Our results show that the caging effect conferred by the ZIF-71 host framework can greatly enhance the thermal stability of the nanoconfined RhB guest molecules.

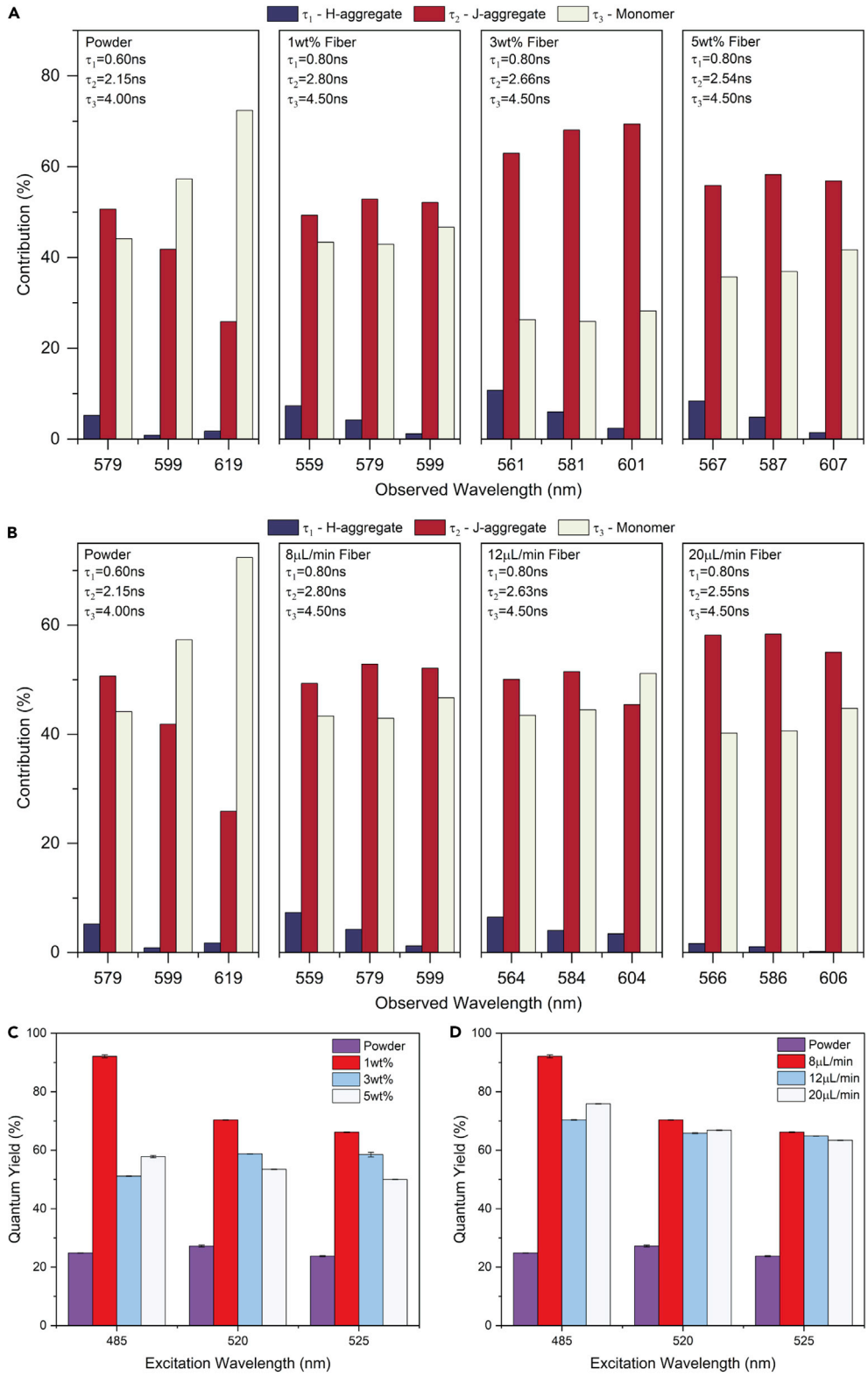

Figure 5. Fluorescent lifetime characteristics and quantum yield of RhB@ZIF-71/PVDF fibers

Contributions = τ_i × normalize pre-exponential factors a_i, $R_t = \Sigma a_i e^{(-t/\tau_i)}$, R_t is the quantity/counts at time t. (A and C) Effects of the different weight percentages and (B and D) the different flow rates.

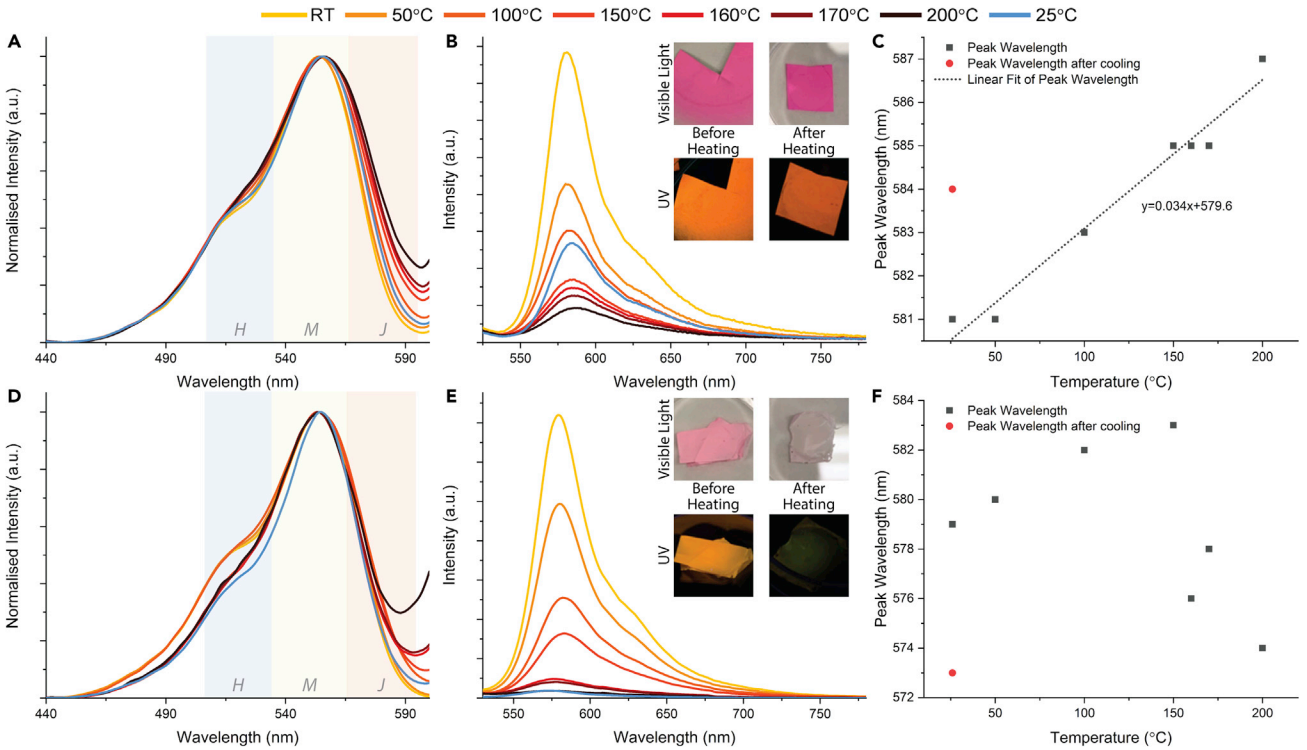

Figure 6. Thermochromism of RhB@ZIF-71/PVDF and RhB/PVDF fibers

Excitation, emission, and peak wavelength changing during heat treatment of (A–C) 1 wt.% RhB@ZIF-71/PVDF fibers and (D–F) RhB/PVDF fibers at different temperatures.

Conclusions

In summary, we report the first example of a thermofluorochromic electrospun fiber comprising a novel Guest@MOF/polymer composite system, termed RhB@ZIF-71/PVDF. We show that it is critical to employ the nanosized crystals of RhB@ZIF-71 (derived from the HCR method) to accomplish a uniform coverage of luminescent crystals dispersed within the polymer matrix. Using fluorescent lifetime spectroscopy, we characterized the interaction of the J-aggregates of RhB between adjacent RhB@ZIF-71 nanocrystals; this mechanism gave the electrospun fiber its luminescence tunability which was subsequently exploited for fluorescent thermometry. Significantly, because the PVDF matrix is helping to greatly reduce the self-absorption effect of RhB@ZIF-71, the composite fiber obtained has a remarkably high QY of ~92%. This value markedly surpasses the typical QY values reported for RhB-based solutions (<66%) and composite solids (<40%). Furthermore, the electrospun composite fibers have achieved enhanced thermal stability under thermal cycling to 200°C and show a notably improved thermochromic performance due to the confinement by the ZIF-71 host. The versatility of electrospinning to tailor composite fiber diameter and architecture combined with the enhanced luminescent sensing properties of the integrated Guest@MOF system bodes well for future engineering applications.

Limitations of the study

RhB@ZIF-71 exhibits multifluorochromic sensing properties which have not been fully investigated in this work apart from its thermofluorochromic effects reported herein. According to the ideas of this article, the fluorescent electrospun fibers with other sensing properties could be further studied.

STAR★METHODS

Detailed methods are provided in the online version of this paper and include the following:

- KEY RESOURCES TABLE
- RESOURCE AVAILABILITY
  - Lead contact

SUPPLEMENTAL INFORMATION

Supplemental information can be found online at https://doi.org/10.1016/j.isci.2021.103035.

ACKNOWLEDGMENTS

This work was supported by the EPSRC Impact Acceleration Account Award (EP/R511742/1) and the ERC Consolidator Grant (PROMOFS grant agreement 771575). We thank the Research Complex at Harwell (RCaH) for the provision of a range of material characterization facilities. We acknowledge Dr. Cyril Besnard and Professor. Alexander M. Korsunsky for the acquisition of the FESEM images.

AUTHOR CONTRIBUTIONS

Conceptualization, Y.Z. and J.-C.T.; methodology, Y.Z. and J.-C.T.; investigation, Y.Z.; writing – original draft, Y.Z.; writing – review & editing, Y.Z. and J.-C.T.; supervision, J.-C.T.

DECLARATION OF INTERESTS

The authors declare no competing interests.

Received: June 23, 2021
Revised: August 3, 2021
Accepted: August 20, 2021
Published: September 24, 2021

REFERENCES

Aguilera-Sigalat, J., and Bradshaw, D. (2016). Synthesis and applications of metal-organic framework–quantum dot (QD@MOF) composites. Coord. Chem. Rev. *307*, 267–291.

Ahmed, R.M., and Saif, M. (2013). Optical properties of rhodamine B dye doped in transparent polymers for sensor application. Chin. J. Phys. *51*, 511–521.

Allendorf, M.D., Foster, M.E., Leonard, F., Stavila, V., Feng, P.L., Doty, F.P., Leong, K., Ma, E.Y., Johnston, S.R., and Talin, A.A. (2015). Guest-induced emergent properties in metal-organic frameworks. J. Phys. Chem. Lett. *6*, 1182–1195.

Asadi, F., Azizi, S.N., and Chaichi, M.J. (2019). Green synthesis of fluorescent PEG-ZnS QDs encapsulated into Co-MOFs as an effective sensor for ultrasensitive detection of copper ions in tap water. Mater. Sci. Eng. C Mater. Biol. Appl. *105*, 110058.

Bai, J.Y., Liu, Y., Hou, Y.J., and Wang, S.H. (2018). Electrospinning preparation and luminescence properties of $Eu_2(PBT)_3(NO_3)_3$/PMMA composite nanofibers. Mater. Chem. Phys. *217*, 486–492.

Chaudhari, A.K., Kim, H.J., Han, I., and Tan, J.C. (2017). Optochemically responsive 2D nanosheets of a 3D metal-organic framework material. Adv. Mater. *29*, 1701463.

Chaudhari, A.K., and Tan, J.C. (2018). Mechanochromic MOF nanoplates: spatial molecular isolation of light-emitting guests in a sodalite framework structure. Nanoscale *10*, 3953–3960.

Chaudhari, A.K., and Tan, J.C. (2020). Dual-guest functionalized zeolitic imidazolate framework-8 for 3D printing white light-emitting composites. Adv. Opt. Mater. *8*, 1901912.

Cui, Y., Yue, Y., Qian, G., and Chen, B. (2012). Luminescent functional metal-organic frameworks. Chem. Rev. *112*, 1126–1162.

Dolgopolova, E.A., Rice, A.M., Martin, C.R., and Shustova, N.B. (2018). Photochemistry and photophysics of MOFs: steps towards MOF-based sensing enhancements. Chem. Soc. Rev. *47*, 4710–4728.

Dong, M.J., Zhao, M., Ou, S., Zou, C., and Wu, C.D. (2014). A luminescent dye@MOF platform: emission fingerprint relationships of volatile organic molecules. Angew. Chem. Int. Ed. *53*, 1575–1579.

Easun, T.L., Moreau, F., Yan, Y., Yang, S., and Schroder, M. (2017). Structural and dynamic studies of substrate binding in porous metal-organic frameworks. Chem. Soc. Rev. *46*, 239–274.

Flyagina, I.S., Mahdi, E.M., Titov, K., and Tan, J.-C. (2017). Thermo-mechanical properties of mixed-matrix membranes encompassing zeolitic imidazolate framework-90 and polyvinylidine difluoride: ZIF-90/PVDF nanocomposites. APL Mater. *5*, 086104.

Fu, H.-R., Yan, L.-B., Wu, N.-T., Ma, L.-F., and Zang, S.-Q. (2018). Dual-emission MOF⊃Dye sensor for ratiometric fluorescence recognition of RDX and detection of a broad class of nitro-compounds. J. Mater. Chem. A. *6*, 9183–9191.

Gutiérrez, M., Martín, C., Van Der Auweraer, M., Hofkens, J., and Tan, J.C. (2020). Electroluminescent guest@MOF nanoparticles for thin film optoelectronics and solid-state lighting. Adv. Opt. Mater. *8*, 2000670.

Gutiérrez, M., Moslein, A.F., and Tan, J.C. (2021). Facile and fast transformation of nonluminescent to highly luminescent metal-organic frameworks: acetone sensing for diabetes diagnosis and lead capture from polluted water. ACS Appl. Mater. Inter. *13*, 7801–7811.

Hao, J.N., and Yan, B. (2015). A water-stable lanthanide-functionalized MOF as a highly selective and sensitive fluorescent probe for Cd^{2+}. ChemComm *51*, 7737–7740.

Heine, J., and Muller-Buschbaum, K. (2013). Engineering metal-based luminescence in

coordination polymers and metal-organic frameworks. Chem. Soc. Rev. *42*, 9232–9242.

Hinckley, D.A., Seybold, P.G., and Borris, D.P. (1986). Solvatochromism and thermochromism of rhodamine solutions. Spectrochim. Acta *42*, 747–754.

Kamtekar, K.T., Monkman, A.P., and Bryce, M.R. (2010). Recent advances in white organic light-emitting materials and devices (WOLEDs). Adv. Mater. *22*, 572–582.

Kanagaraj, S., Puthanveedu, A., and Choe, Y. (2019). Small molecules in light-emitting electrochemical cells: promising light-emitting materials. Adv. Funct. Mater. *30*, 1907126.

Khader, M.A. (2008). Lasing characteristics of rhodamine B and rhodamine 6G as a sensitizer in sol–gel silica. Opt. Laser Technol. *40*, 445–452.

Li, J., Yuan, S., Qin, J.S., Pang, J., Zhang, P., Zhang, Y., Huang, Y., Drake, H.F., Liu, W.R., and Zhou, H.C. (2020). Stepwise assembly of turn-on fluorescence sensors in multicomponent metal-organic frameworks for in vitro cyanide detection. Angew. Chem. Int. Ed. *59*, 9319–9323.

Lin, R.-B., Xiang, S., Li, B., Cui, Y., Qian, G., Zhou, W., and Chen, B. (2019). Our journey of developing multifunctional metal-organic frameworks. Coord. Chem. Rev. *384*, 21–36.

Luo, T.Y., Das, P., White, D.L., Liu, C., Star, A., and Rosi, N.L. (2020). Luminescence "Turn-On" detection of gossypol using In^{3+}-based metal-organic frameworks and Ln^{3+} salts. J. Am. Chem. Soc. *142*, 2897–2904.

Lustig, W.P., Mukherjee, S., Rudd, N.D., Desai, A.V., Li, J., and Ghosh, S.K. (2017). Metal-organic frameworks: functional luminescent and photonic materials for sensing applications. Chem. Soc. Rev. *46*, 3242–3285.

Mieno, H., Kabe, R., Notsuka, N., Allendorf, M.D., and Adachi, C. (2016). Long-lived room-temperature phosphorescence of coronene in zeolitic imidazolate framework ZIF-8. Adv. Opt. Mater. *4*, 1015–1021.

Mollick, S., Mandal, T.N., Jana, A., Fajal, S., Desai, A.V., and Ghosh, S.K. (2019). Ultrastable luminescent hybrid bromide perovskite@MOF nanocomposites for the degradation of organic pollutants in water. ACS Appl. Nano Mater. *2*, 1333–1340.

Nauruzbayeva, J., Sun, Z., Gallo, A., Jr., Ibrahim, M., Santamarina, J.C., and Mishra, H. (2020). Electrification at water-hydrophobe interfaces. Nat. Commun. *11*, 5285.

Phan, A., Doonan, C.J., Uribe-Romo, F.J., Knobler, C.B., O'keeffe, M., and Yaghi, O.M. (2010). Synthesis, structure, and carbon dioxide capture properties of zeolitic imidazolate frameworks. Acc. Chem. Res. *43*, 58–67.

Qin, S.-J., and Yan, B. (2018). Dual-emissive ratiometric fluorescent probe based on Eu^{3+}/C-dots@MOF hybrids for the biomarker diaminotoluene sensing. Sens. Actuator B Chem. *272*, 510–517.

Sagoo, S.K., and Jockusch, R.A. (2011). The fluorescence properties of cationic rhodamine B in the gas phase. J. Photochem. Photobiol. A *220*, 173–178.

Stassen, I., Burtch, N., Talin, A., Falcaro, P., Allendorf, M., and Ameloot, R. (2017). An updated roadmap for the integration of metal-organic frameworks with electronic devices and chemical sensors. Chem. Soc. Rev. *46*, 3185–3241.

Stobiecka, M., and Hepel, M. (2011). Multimodal coupling of optical transitions and plasmonic oscillations in rhodamine B modified gold nanoparticles. Phys. Chem. Chem. Phys. *13*, 1131–1139.

Takashima, Y., Martinez, V.M., Furukawa, S., Kondo, M., Shimomura, S., Uehara, H., Nakahama, M., Sugimoto, K., and Kitagawa, S. (2011). Molecular decoding using luminescence from an entangled porous framework. Nat. Commun. *2*, 168.

Tang, Y., He, W., Lu, Y., Fielden, J., Xiang, X., and Yan, D. (2014). Assembly of ruthenium-based Complex into metal–organic framework with tunable area-selected luminescence and enhanced photon-to-electron conversion efficiency. J. Phys. Chem. C *118*, 25365–25373.

Titov, K., and Tan, J.-C. (2016). Facile patterning of electrospun polymer fibers enabled by electrostatic lensing interactions. APL Mater. *4*, 086107.

Wang, J., Zhang, Y., Yu, Y., Ye, F., Feng, Z., Huang, Z., Liu, X., and Zhou, X. (2019). Spectrally flat white light emission based on red-yellow-green-blue dye-loaded metal-organic frameworks. Opt. Mater. *89*, 209–213.

Yao, C.X., Zhao, N., Liu, J.C., Chen, L.J., Liu, J.M., Fang, G.Z., and Wang, S. (2020). Recent progress on luminescent metal-organic framework-involved hybrid materials for rapid determination of contaminants in environment and food. Polymers *12*, 691.

Yin, H., Khosravi, A., O'connor, L., Tagaban, A.Q., Wilson, L., Houck, B., Liu, Q., and Lind, M.L. (2017). Effect of ZIF-71 particle size on free-standing ZIF-71/PDMS composite membrane performances for ethanol and 1-butanol removal from water through pervaporation. Ind. Eng. Chem. Res. *56*, 9167–9176.

Yoo, J., Ryu, U., Kwon, W., and Choi, K.M. (2019). A multi-dye containing MOF for the ratiometric detection and simultaneous removal of $Cr_2O_7^{2-}$ in the presence of interfering ions. Sens. Actuator B Chem. *283*, 426–433.

Zhang, H., Song, H., Yu, H., Li, S., Bai, X., Pan, G., Dai, Q., Wang, T., Li, W., Lu, S., et al. (2007). Modified photoluminescence properties of rare-earth complex/polymer composite fibers prepared by electrospinning. Appl. Phys. Lett. *90*, 103103.

Zhang, Y., Gutiérrez, M., Chaudhari, A.K., and Tan, J.C. (2020). Dye-encapsulated zeolitic imidazolate framework (ZIF-71) for fluorochromic sensing of pressure, temperature, and volatile solvents. ACS Appl. Mater. Inter. *12*, 37477–37488.

Zhao, H., Ni, J., Zhang, J.J., Liu, S.Q., Sun, Y.J., Zhou, H., Li, Y.Q., and Duan, C.Y. (2018). A trichromatic MOF composite for multidimensional ratiometric luminescent sensing. Chem. Sci. *9*, 2918–2926.

STAR★METHODS

KEY RESOURCES TABLE

REAGENT or RESOURCE	SOURCE	IDENTIFIER
Chemicals, peptides, and recombinant proteins		
4,5-Dichloroimidazole	Alfa Aesar	CAS: 15965-30-7
Triethylamine	Alfa Aesar	CAS: 121-44-8
Rhodamine B	Alfa Aesar	CAS: 81-88-9
Zinc acetate dihydrate	Thermo Fisher Scientific	CAS: 5970-45-6
HSV900 poly(vinylidene fluoride)	Kynar	CAS: 24937-79-9
Deposited data		
ZIF-71 crystal structure	(Phan et al., 2010)	CCDC code: GITVIP

RESOURCE AVAILABILITY

Lead contact

Further information and requests for resources and reagents should be directed to and will be fulfilled by the lead contact, Prof. Jin-Chong Tan (jin-chong.tan@eng.ox.ac.uk).

Materials availability

Raw materials used in the study are commercially available.

Data and code availability

This study did not generate computer code. All data and analytical methods are available in the main text or in supplemental information section. The ZIF-71 crystal structure data used is from The Cambridge Crystallographic Data Center (CCDC code: GITVIP). Any additional information required to reanalyze the data reported in this paper is available from the lead contact upon request.

METHOD DETAILS

Synthesis of RhB@ZIF-71 by using HCR method

15 mL methanol solution of 4,5-dichloroimidazole (dcIm, 9.6 mmol) plus triethylamine (NEt_3, 9.6 mmol) was combined with 1 mL methanol solution of rhodamine B (RhB, 0.05 mmol). After the combination, 15 mL clear solution of zinc acetate (2.4 mmol) was immediately added into the mixture, producing a sol-like product. Then the product was washed thoroughly three times using methanol to remove the guests adhered to the MOF surface. The nanocrystals of RhB@ZIF-71 were separated from the suspension by centrifugation at 8000 rpm for 10 min.

Preparation of RhB@ZIF-71 and RhB in PVDF solution

The electrospinning polymer solution was prepared by dissolving 15 g HSV900 polyvinylidene fluoride (PVDF) powder in 94 g dimethylacetamide (DMA), to yield 13.7 wt.% PVDF in DMA. Then the appropriate amount of RhB@ZIF-71 in acetone solution was added to the PVDF in DMA solution to make the mass ratio of RhB@ZIF-71 to PVDF of 1:99, 3:97, 5:95 and the volume ratio of DMA to acetone was 3:1. According to the Beer-Lambert Law, an acetone solution of RhB with the same absorbance as RhB@ZIF-71 acetone solution was prepared (Figure S9), and then the RhB acetone solution with the same weight as RhB@ZIF-71 acetone solution was used to mix with PVDF.

Electrospinning

Electrospinning was carried out at 10.5 kV from a DC high-voltage generator. The PVDF solution was supplied to a G19 needle emitter (nozzle) with a blunt tip via a syringe pump at a processing rate of 8–20 μL/min. The distance from the collector (aluminum foil or diamond-shaped mesh) to the tip was 16 cm. Further details about the formation of the textured mat by electrospinning can be found in ref

(Titov and Tan, 2016), where they described the application of electrostatic lensing interaction to fabricate fibers with predefined orientations mirroring the architecture of a conductive wire mesh.

Materials characterization

The structures and morphologies were examined under scanning electron microscopy (SEM; Hitachi TM3030Plus and $LYRA_3$ GM TESCAN) and an atomic force microscope (Neaspec s-SNOM under tapping mode). The PXRD pattern was recorded using a Rigaku MiniFlex with a Cu Kα source (1.541 Å). UV-2600 UV-Vis diffuse reflectance spectrophotometer (Shimadzu) equipped with an integrating sphere was used to measure the reflectance spectra of the solid samples. The melting temperatures were measured by using TA Instruments DSC Q2000. ATR-FTIR absorption spectra were recorded by using a Nicolet iS10 FTIR spectrometer. An FS5 spectrofluorometer (Edinburgh Instruments) equipped with different accessories was used to measure the steady-state emission and excitation spectra, quantum yield (QY), fluorescent lifetime by time-correlated single-photon counting (TCSPC), and thermochromic response.